Response to Community Comment (Liping Liu)

We sincerely thank Dr. Liping Liu for the thorough and constructive community comment. These suggestions have substantially improved the clarity, rigor, and presentation of our manuscript. Below we address each point in detail. Reviewer comments are shown in italic and our responses in bold.

General comments

1. The theoretical derivation (Eqs. 3–7) assumes that fog droplet size distribution (DSD) follows a lognormal distribution. The authors briefly mention bimodal/multimodal DSD as a limitation for future work in the conclusion, without any assessment of its prevalence or impact on algorithm performance. This may undermine the reliability of the methodology. The authors may need to provide a statistical analysis of the occurrence frequency and characteristics of bimodal/multimodal DSD in the 5-year FM-120 dataset collected at the Data Observation Base, discuss the physical mechanism by which bimodal DSD disrupts the coupling relationships between radar reflectivity (Z), liquid water content (LWC), geometric mean radius (rm), and extinction coefficient (βext), and clearly define the applicability boundary of the proposed algorithm under non-lognormal DSD conditions.

Response: We thank Dr. Liu for this insightful comment. We fully agree that the prevalence and impact of bimodal DSD deserve thorough quantitative assessment rather than a brief mention in the conclusion.

In the revised manuscript, we have conducted a comprehensive statistical analysis of the spectral-regime dataset from the 5-year (2019–2023) FM-120 record. Each 1-min spectrum was assigned one of four hard shape labels (broad-unimodal, narrow-unimodal, bimodal, uncertain) following objective morphological criteria. After quality control, the spectral-regime dataset aggregates 236,037 contributing 1-Hz records into 4,234 valid 1-min spectra from 28 events.

The results show that bimodal spectra account for 6.38% of all valid minutes across the full spectral-regime dataset. However, their prevalence is strongly visibility-dependent. Within the DSD-derived visibility domain, the event-balanced bimodal fraction rises to 24.07% (95% complete-event-bootstrap interval: 9.11–40.04%) at 100–200 m visibility, compared with 4.22% (1.45–7.96%) at 200–500 m and 0.77% (0.03–1.79%) at 500–

1,000 m. Only three events contribute to the 50–100 m bin, where the interval spans 0–100%, and no spectra occur at 0–50 m. These statistics are now presented in Section 3.1 and the revised Fig. 3.

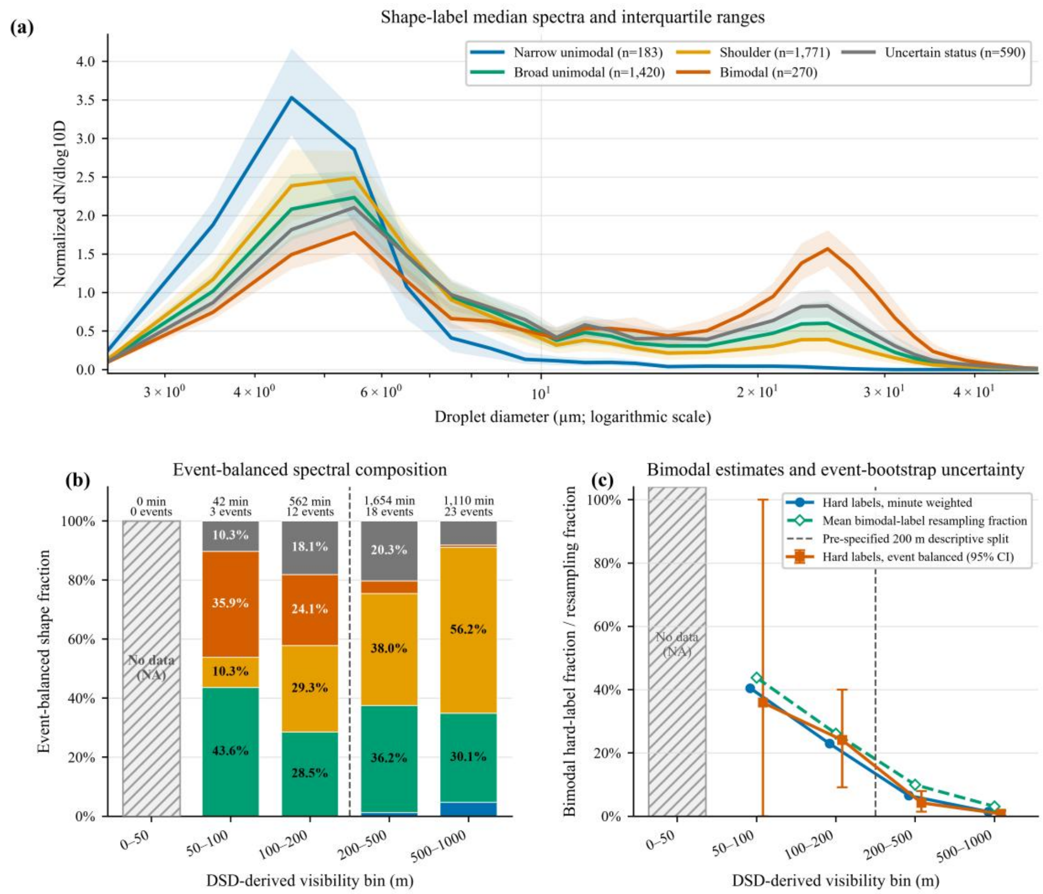

Figure R1. Revised version of Fig. 3 in the manuscript (spectral-regime characterization).Data source: FM-120 spectral-regime dataset comprising 4234 valid 1-min spectra from 28 fog events (2019–2023) at the Datan Observation Base. Method: each spectrum was classified into one of four shape categories (narrow unimodal, broad unimodal, shoulder, bimodal) or an uncertain status; event-balanced hard-label fractions were computed in DSD-derived visibility bins ([0,50), [50,100), [100,200), [200,500), [500,1000) m), with 95% intervals from 1000 complete-event resamples.

Regarding the physical mechanism: separated spectral modes or sparse larger droplets alter the DSD moments controlling reflectivity (sixth moment), LWC (third moment), and extinction (second moment weighted by Qext) in different ways, thereby weakening the single-lognormal closure that links these quantities through shared NT and σ. Specifically, a secondary mode at larger radii preferentially boosts the sixth moment (Z) relative to the third moment (LWC), breaking the moment coupling assumed in Eq. (9). This causes the extinction-oriented radius–reflectivity parameterization (Eq. 14) to produce biased extinction estimates in bimodal-dominated regimes.

The applicability boundary is now clearly defined: the proposed algorithm is designed for liquid, non-precipitating fog where the DSD can be reasonably approximated by a single lognormal distribution. Section 6 (Conclusions) now explicitly states that bimodal spectra become increasingly prevalent below 200 m visibility, and that the extinction-oriented parameterization developed in Section 3.3 mitigates—but does not eliminate—the systematic errors introduced by non-lognormal DSD. The signed-residual analysis in Section 4.1 quantifies the magnitude of this structural bias, as illustrated in Figure R2.

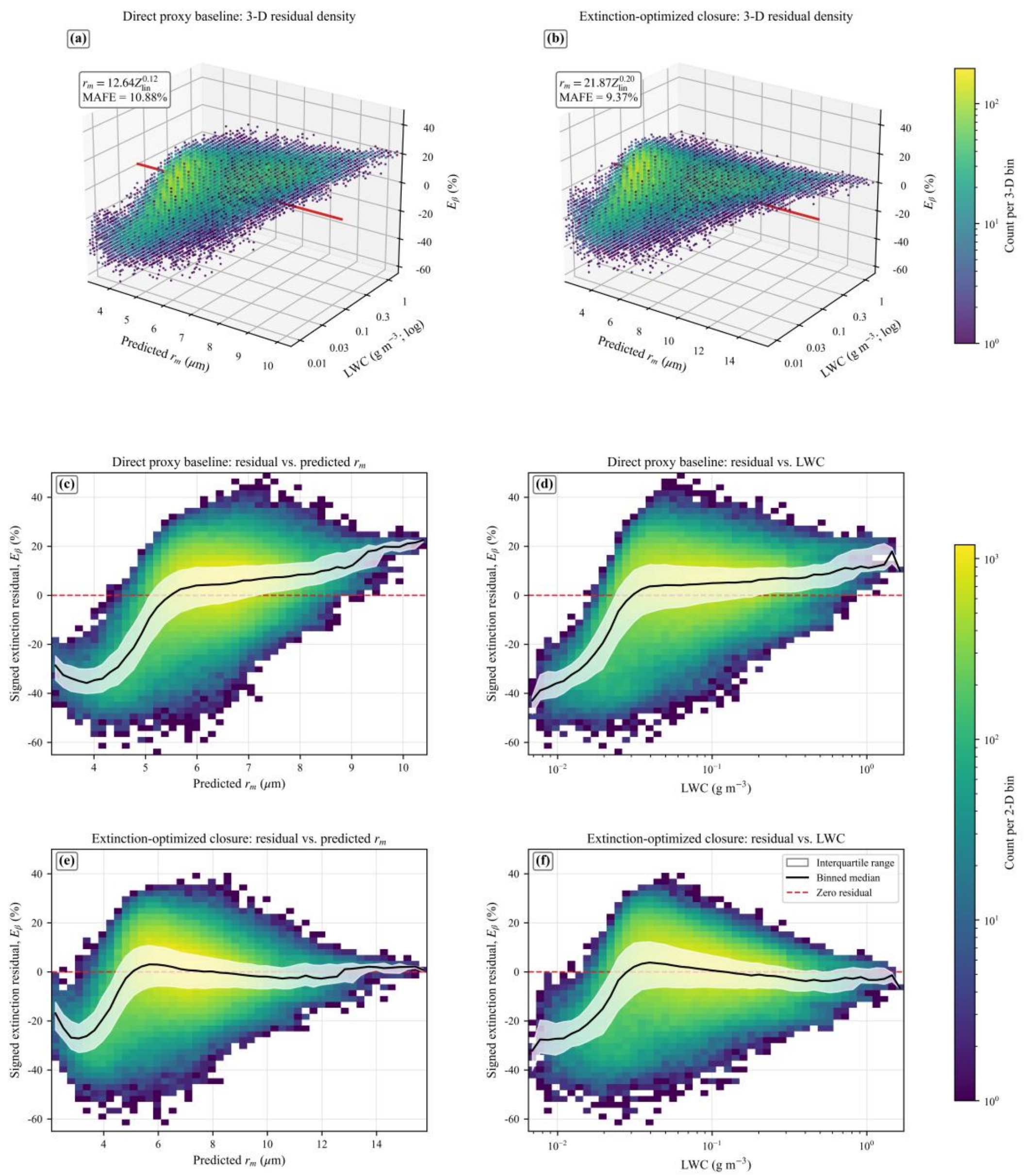

Figure R2. Revised version of Fig. 6 in the manuscript (extinction residual analysis). Data source: moment-closure development dataset (188214 rows) co-derived from FM-120 DSD observations at the Datan Observation Base, containing Z, LWC, rm pseudo-targets, and Mie extinction references. Signed fractional extinction residuals $E_\beta = (\beta_{closed} - \beta_{Mie})/\beta_{Mie} \times 100\%$ were computed for both the direct r_m–Z relation and the extinction-oriented relation; 3-D residual density and 2-D projections against predicted rm and LWC are shown with binned medians and interquartile ranges.

2. The authors adopt the LWC retrieval algorithm from Ge et al. (2023), which was originally developed for general liquid water clouds. Sea fog exhibits distinct microphysical characteristics compared to clouds, including smaller droplet sizes, lower LWC values, and shallower vertical extents, which may significantly affect algorithm performance. The authors can describe in detail all adaptations made to the original LWC algorithm specifically for sea fog conditions, particularly the 10-bin segmentation method mentioned in Section 3.1.

Response: We thank Dr. Liu for raising this important point regarding algorithm adaptation. We agree that the differences between sea fog and general liquid clouds necessitate specific adaptations.

In the revised manuscript, Section 3.2 now provides a detailed description of all adaptations made to the Ge et al. (2023) LWC retrieval framework for sea fog conditions. The key adaptations are as follows:

(1) 10-bin segmentation. The original algorithm used a fixed-segment approach. Given the substantial variability in liquid water path (LWP) along fog profiles—as documented in Section 3.1—we apply a 10-bin segmentation approach that partitions the fog profile into segments such that the LWP of each segment falls within the bounds prescribed by the trust-region reflective (TRR) least-squares solver (Cartis et al., 2009). Each segment is fitted independently, with the accumulated attenuation derived from the retrieved LWC applied to correct its reflectivity prior to fitting. This adaptive segmentation accommodates the shallower vertical extents (typically < 500 m) and sharper LWP gradients characteristic of sea fog.

(2) Starting-vector stratification. The original algorithm used a single starting vector for all cloud types. For sea fog, we introduced a dual-branch initialization based on the maximum reflectivity within each segment: for a maximum not exceeding −15 dBZ, the starting vector is [0.5, 0.01, 1]; for a maximum greater than −15 dBZ, it is [0.5, 0.01, 0.1]. Both branches use lower bounds [0, 0, 0] and upper bounds [1, 1, 10].

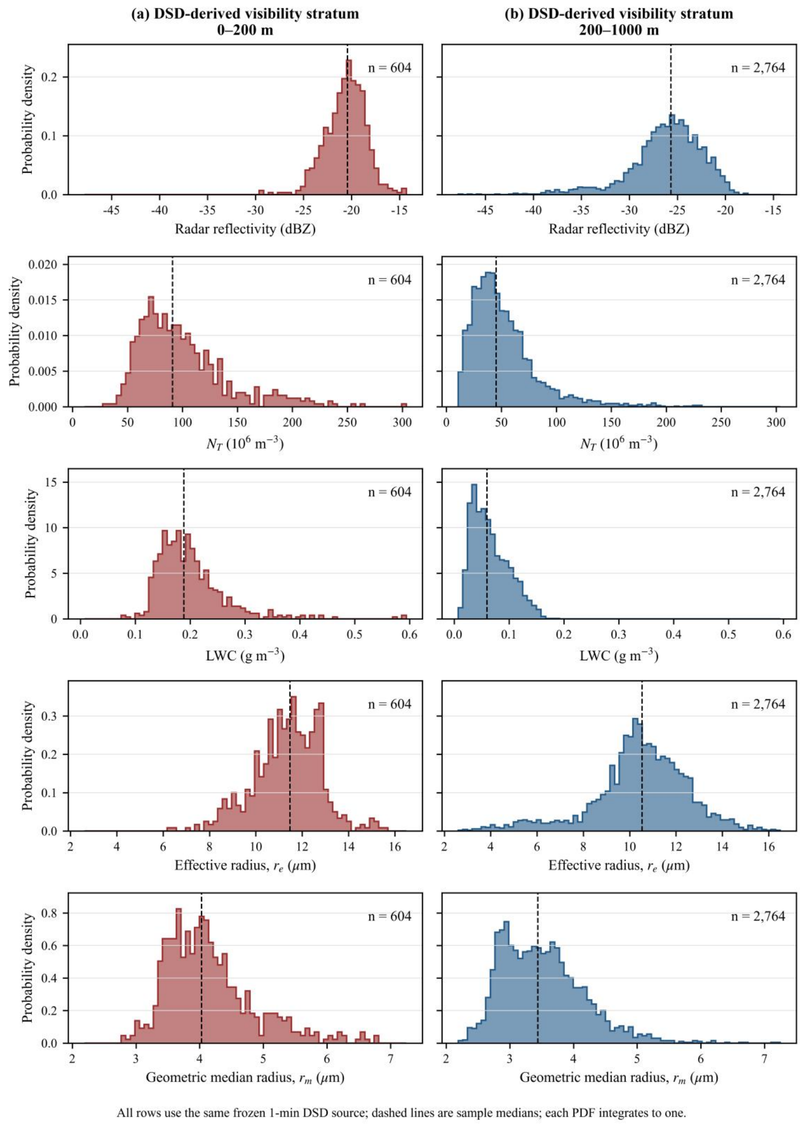

Figure R5. Revised version of Fig. 4 in the manuscript (parameter distributions). Timestamp-resolved parameter-distribution dataset derived from FM-120 DSD observations (2019–2023) at the Datan Observation Base, comprising 188128 unique timestamps stratified by DSD-derived visibility at 0–200 m and 200–1000 m. FM-120/DSD-derived radar-equivalent reflectivity (dBZ), total number concentration (N_T), liquid water content (LWC), effective radius (r_e), and geometric median radius (r_m) were computed as discrete DSD sums at each timestamp; histograms normalized within each stratum with dashed median lines.

3. The authors state that "Doppler and ground clutter suppression techniques are further employed to eliminate ground clutter effects" (Section 2) without details on the specific algorithms used, parameter settings, or effectiveness evaluation. The authors should describe the exact clutter suppression algorithms used and their specific parameter settings.

Response: We thank Dr. Liu for requesting these important technical details. The ground-clutter suppression adopts a clutter-map subtraction approach. Because our mass-absorption-based retrieval places high demands on data continuity, we recorded ground-clutter signatures under clear-sky conditions to construct a static clutter map, which was subsequently subtracted from the measured reflectivity to complete the ground-clutter removal (Kanemaru et al., 2021). We present in Fig. X a direct comparison of radar reflectivity before and after clutter filtering for the sea-fog event on 2 March 2025. Panel (a) shows the original reflectivity contaminated by persistent ground clutter, evident as spurious high-reflectivity returns near the surface (below approximately 1 km) and along certain azimuths. Panel (b) confirms that after clutter filtering, these non-meteorological near-surface returns are largely eliminated, while the fog echo structure aloft is preserved with minimal distortion. The result provides a reliable, clutter-free reflectivity field for the subsequent visibility retrieval.

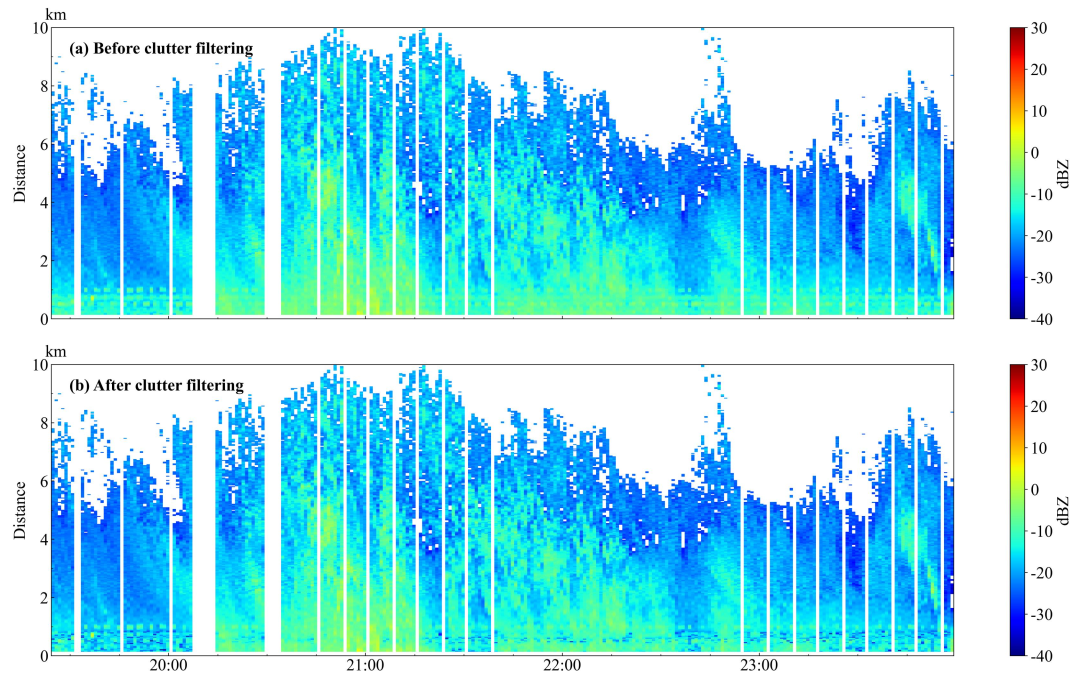

Figure R4. Ground-clutter filtering effectiveness for the 2 March 2025 sea-fog case. YLUKA2 Ka-band radar observations along the 150-degree azimuth at the Datan Observation Base, showing the time-range evolution from 19:30 to 23:30 LST.Ground-clutter suppression by subtracting a clear-sky clutter map (Kanemaru et al., 2021).

Minor points and comments

1. Define all symbols on their first use in the text, including K and the constant c in Eq. (11).*

Response: We thank Dr. Liu for this suggestion. All symbols are now defined on first use in the revised manuscript. Specifically, K* is defined in Section 3.2 as the mass-absorption coefficient determined by the radar wavelength, temperature, and complex refractive index of cloud droplets, which is treated as a constant for the Ka-band radar operating at a fixed wavelength. The constant c in Eq. (12) is defined as the prefactor of the segment-wise power-law closure relation, whose value is optimized by the trust-region reflective (TRR) solver for each range segment. The exponent b is defined as the corresponding power-law exponent, also optimized segment-wise.

2. Improve the discrimination of the legend lines in Figure 7(e) and directly label the fractional error of each retrieval method within the figure.

Response: We thank Dr. Liu for this practical suggestion. In the revised Figure 9(e) (formerly Fig. 7e), we have used distinct line styles (solid, dashed, dotted, and dash-dotted) and colour-coded labels to improve visual discrimination. The present retrieval achieves MAE = 0.092 km and RE = 42.86%; the local FM-120 relation achieves MAE = 0.123 km and RE = 50.53%; Liu et al. (2019) achieves MAE = 0.160 km and RE = 85.30%; and Gultepe et al. (2009) shows the largest departure with MAE = 0.533 km and RE = 310.63%. The local-consistency comparison is shown in Figure R4.

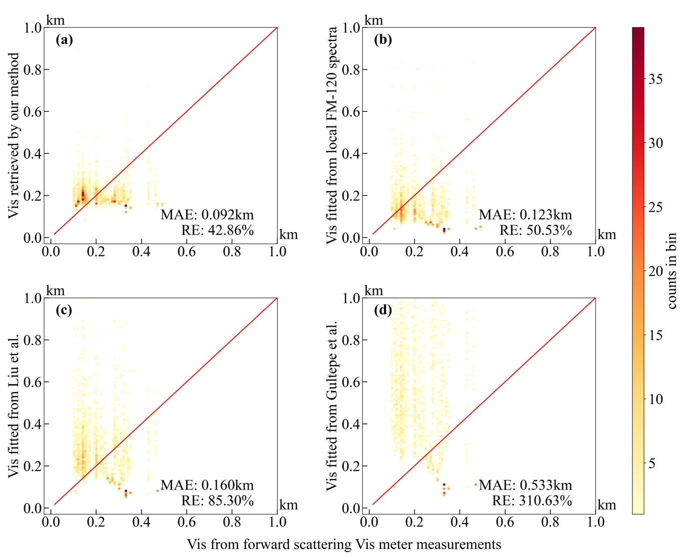

Figure R5. Revised version of Fig. 10 in the manuscript (consistency between retrieval and observation). Data source: ten criterion-selected spring 2025 fog events (DNQ3 visibility < 1000 m for at least 30 min) observed with the YLUKA2 Ka-band radar and DNQ3 forward-scatter visibility meter at the Datan Observation Base. Method: radar-derived visibility from the ~300-m range gate along the 150-degree azimuth was compared against co-located DNQ3 measurements and three empirical Vis–Z relations (the local FM-120 exponential relation, Liu et al. 2019, and Gultepe et al. 2009); axes in km with 1:1 reference lines.

3. Add a new table summarizing the basic characteristics of the 10 validation sea fog events, including start/end time, minimum visibility, maximum LWC, and fog type.

Response: We thank Dr. Liu for this suggestion. A summary table (Table R1) of the ten spring-2025 DNQ3-selected low-visibility cases has been added to the revised manuscript (Section 5). The table includes event number, period (LST), duration, minimum visibility, temperature, wind speed, wind direction, and relative humidity. All ten events are advection sea fog cases selected under strict criteria.

4. Revise the sentence "thereby avoiding purely empirical formulations" in the abstract to "thereby reducing reliance on purely empirical site-specific formulations" for greater accuracy.

Response: We thank Dr. Liu for this precise wording suggestion. The sentence has been revised exactly as suggested. The abstract now reads: "…thereby reducing reliance on purely empirical site-specific formulations." This revision accurately reflects the fact that the extinction-oriented parameterization, while physically motivated, is still calibrated against same-source FM-120 DSD observations and is not entirely free of empirical elements.

5. Replace "global scale" with "near-global scale" when referring to satellite observations in Section 1, as satellite sensors do not provide complete coverage of the polar regions.

Response: We thank Dr. Liu for this correction. "Global scale" has been replaced with "near-global scale" in Section 1 to accurately reflect the spatial coverage limitations of satellite-based observations, particularly the incomplete coverage of polar regions.

6. Provide a brief definition of the trust region reflection (TRR) algorithm or add a relevant reference in Section 3.1 for readers unfamiliar with this optimization method.

Response: We thank Dr. Liu for this suggestion. A brief definition and the key reference have been added to Section 3.2. The trust-region reflective (TRR) algorithm is a nonlinear least-squares optimization method that iteratively solves a constrained quadratic model of the objective function within a trust region around the current iterate (Cartis et al., 2009). The method is particularly suited for problems with bound constraints, as it ensures that the parameter vector remains within physically meaningful bounds during optimization. The citation to Cartis et al. (2009) has been added to the reference list.

7. Revise the overclaim "applies to diverse fog types" in Section 6 to "shows promise for application to diverse fog types, pending further validation" since the method has only been tested on advection sea fog.

Response: We thank Dr. Liu for this important caution. The statement has been revised exactly as suggested. Section 6 (Conclusions) now reads: "…shows promise for application to diverse fog types, pending further validation." We agree that the current validation is limited to advection sea fog cases at a single coastal site, and broader applicability across radiation fog, mixing fog, and other fog types requires additional datasets and evaluation.

8. Discuss whether the overall fractional error of 36.61% meets the accuracy requirements for operational fog early warning in the transportation and maritime sectors in Section 4.

Response: We thank Dr. Liu for this important question regarding operational applicability, which is now addressed in the revised Section 5.

We first clarify that the fractional error of 36.61% referenced by Dr. Liu has been superseded in the updated manuscript. The mean absolute error (MAE) and relative error (RE) for the ten-event comparison are: the present retrieval achieves MAE = 0.092 km and RE = 42.86%; the local FM-120 relation achieves MAE = 0.123 km and RE = 50.53%; Liu et al. (2019) achieves MAE = 0.160 km and RE = 85.30%; and Gultepe et al. (2009) departs most strongly with MAE = 0.533 km and RE = 310.63%.

Regarding operational requirements: the World Meteorological Organization (WMO) does not prescribe a single visibility-retrieval accuracy threshold for operational fog warnings; instead, the key requirement is correct classification of visibility into warning-relevant categories (e.g., < 200 m for dense fog alerts, < 500 m for aviation minimums). The present retrieval, with a MAE of 92 m, demonstrates category-level discrimination capability within the dense-fog threshold range. However, we acknowledge that the relative error of 42.86% is not yet sufficient for precision-critical applications such as autonomous vessel navigation or runway visual range determination. The revised Section 5 now includes this discussion, noting that the comparison is a local-consistency assessment rather than an independent method-ranking test, and that a stricter quantitative evaluation requires more completely collocated observations over additional fog regimes.

9. Explain the criteria used to select the 10 validation sea fog events and provide a clear definition of what constitutes a fog event in this study in Section 5.

Response: We thank Dr. Liu for requesting this clarification. The event selection criteria and the definition of a fog event are now explicitly stated in the revised Section 5. A fog event is defined as a continuous period during which DNQ3 visibility remains below 1,000 m for at least 30 min, with no precipitation weather occurring during the interval. Events are separated when the gap between consecutive valid low-visibility minutes exceeds 30 min. The ten spring-2025 cases were selected under these strict criteria from the radar–visibility-meter collocated observation record. Table R1 (see response to Comment 3 above) provides the basic characteristics of all ten events.

These selection criteria ensure that: (i) the visibility-meter record provides a reliable reference for consistency comparison; (ii) precipitation contamination is excluded; and (iii) each event has sufficient temporal duration to capture the fog life cycle. The criteria are now documented in Section 2 (instrumentation) and cross-referenced in Section 5.

Response: We once again thank Dr. Liping Liu for the time and expertise devoted to this detailed community comment. All points have been addressed in the revised manuscript, and we believe the revisions have substantially improved the clarity, rigor, and presentation of our work. We hope the revised version now meets the standards for publication in Atmospheric Measurement Techniques.

References

Cartis, C., Figueiredo, M., and Vicente, L. N.: Trust-region and other regularisations of linear least-squares problems, BIT Numer. Math., 49, 21–53, doi:10.1007/s10543-008-0199-2, 2009.

Ge, J., et al.: A Novel Liquid Water Content Retrieval Method Based on Mass Absorption for Single-Wavelength Cloud Radar, IEEE Trans. Geosci. Remote Sens., 61, 4102815, doi:10.1109/TGRS.2023.3278735, 2023.

Gultepe, I., and Coauthors: The Fog Remote Sensing and Modeling Field Project, Bull. Amer. Meteor. Soc., 90, 341–360, doi:10.1175/2008BAMS2354.1, 2009.

Kamangir, H., Krell, E., Collins, W., King, S. A., and Tissot, P.: Importance of 3D convolution and physics on a deep learning coastal fog model, Environ. Model. Softw., 154, 105424, doi:10.1016/j.envsoft.2022.105424, 2022.

Li, Y., Zhang, G., Doviak, R. J., Lei, L., and Cao, Q.: A New Approach to Detect Ground Clutter Mixed With Weather Signals, IEEE Trans. Geosci. Remote Sens., 51, 2373–2387, doi:10.1109/TGRS.2012.2209658, 2013.

Liu, G. P., Huang, S. Y., Liang, Y., et al.: Application of Millimeter Wave Radar in Harbor Marine Fog Observation and Visibility Inversion, J. Arid Meteorol., 37, 993–1004, doi:10.11755/j.issn.1006-7639(2019)-06-0993, 2019.

Table R1. Basic characteristics of the ten spring-2025 DNQ3-selected low-visibility cases.

Event	**Period (LST)**	**Duration (min)**	**Min Vis (m)**	**T (°C)**	**Wind speed (m s^{-1})**	**Wind direction (°)**	**RH (%)**
1	2025-03-02 19:00 – 2025-03-03 05:00	600	156	19.48	3.16	219.80	97.70
2	2025-03-04 00:00 – 02:20	140	462	17.93	1.48	269.90	98.20
3	2025-03-04 05:40 – 06:10	30	563	17.67	3.32	58.10	97.20
4	2025-03-25 00:35 – 07:05	390	101	17.86	2.32	228.40	93.70
5	2025-03-26 02:20 – 08:55	395	134	18.99	3.16	219.40	90.90
6	2025-03-27 01:30 – 07:30	360	139	19.69	3.81	213.90	95.80
7	2025-03-27 20:50 – 2025-03-28 04:50	480	104	21.04	3.48	222.60	94.00
8	2025-04-10 03:25 – 08:20	295	264	20.44	1.97	235.50	96.50
9	2025-04-12 04:15 – 07:35	200	246	22.58	4.53	217.60	92.20
10	2025-04-12 11:15 – 14:40	205	455	23.93	8.05	201.90	96.40

Note: Visibility, temperature, wind speed, wind direction, and relative humidity data are from the Datan Observation Base.